Acta Crystallographica Section A
Foundations of Crystallography
ISSN 0108-7673

Received 3 March 2011
Accepted 30 May 2011

Atomic resolution imaging using the real-space distribution of electrons scattered by a crystalline material

Sorin Lazar,[a,b]* Joanne Etheridge,[c] Christian Dwyer,[c,d] Bert Freitag[a] and Gianluigi A. Botton[b]

[a]FEI Electron Optics, Achtseweg Noord 5, Eindhoven, 5600 KA, The Netherlands, [b]Canadian Centre for Electron Microscopy and Department of Materials Science and Engineering, McMaster University, 1280 Main Street West, Hamilton, Ontario, Canada L8S 4M1, [c]Monash Centre for Electron Microscopy, and Department of Materials Engineering, Monash University, Victoria 3800, Australia, and [d]ARC Centre of Excellence for Design in Light Metals, Monash University, Victoria 3800, Australia. Correspondence e-mail: sorin.lazar@fei.com

We present an alternative atomic resolution incoherent imaging technique derived from scanning transmission electron microscopy (STEM) using detectors in real space, in contrast to conventional STEM that uses detectors in diffraction space. The images obtained from various specimens have a resolution comparable to conventional high-angle annular dark-field (HAADF) STEM with good contrast, which seems to be very robust with respect to thickness, focus and imaging conditions. The results of the simulations are consistent with the experimental results and support the interpretation of the real-space STEM image contrast as being a result of aberration-induced displacements of the high-angle scattered electrons.

1. Introduction

In the field of transmission electron microscopy (TEM), recent developments of electron-optical aberration correctors (Haider, Uhlemann *et al.*, 1998; Krivanek *et al.*, 1999) and exceptional instrumental stability have led to major advances in our ability to probe the atomic structure of matter. For example, spatial resolutions approaching 0.5 Å have now been demonstrated in both phase-contrast TEM and incoherent high-angle annular dark-field (HAADF) scanning transmission electron microscopy (STEM) (Kisielowski *et al.*, 2008; Haider, Uhlemann *et al.*, 1998; Nellist *et al.*, 2004; Sawada *et al.*, 2007; Erni *et al.*, 2009; Krivanek *et al.*, 2010). In addition to enabling unprecedented sensitivity and precision in the characterization of materials, such advances in instrumentation also inspire the development of new imaging methods that address the limitations of old ones, offering the potential for an even greater impact in materials research. For example, new imaging methods with enhanced sensitivity to light atoms have recently been developed for both TEM and STEM modes (Jia & Urban, 2004; Jia *et al.*, 2005; Findlay *et al.*, 2009, 2010). Moreover, the flexibility of modern instruments makes it possible to devise hybrid methods that combine the advantages of several techniques.

Here we explore the possibility of using a double-aberration-corrected TEM/STEM to develop an alternative imaging mode capable of incoherent atomic resolution imaging. This mode utilizes a STEM configuration with the electron detectors (disc and annular) situated in the conjugate image plane instead of the diffraction plane. This enables an incoherent atomic resolution image to be generated using the disc detector with similar characteristics to conventional HAADF-STEM, but with significantly greater intensity. Furthermore, it provides the possibility of correlating the position of the probe on the specimen with other signals that can be recorded in the image plane. This technique, here referred to as real-space STEM (R-STEM), is shown to be reliable over a range of specimen thicknesses and applicable to a broad range of materials. The potential applications of R-STEM include low-dose STEM imaging and simultaneous energy-dispersive X-ray (EDX) chemical mapping.

2. Experimental results

In conventional STEM imaging, a small electron probe is raster-scanned across a specimen while the transmitted signal is recorded at each point of the raster. The transmitted signal is measured in the diffraction plane, typically using a disc- or annular-shaped detector (Crewe *et al.*, 1968), and is representative of electrons that have been scattered by the specimen into a specific angular range (Fig. 1*a*). In contrast, the signal in R-STEM is recorded in the image plane, also using a disc- and annular-shaped detector, and so is representative of the transverse position of the scattered electrons (Fig. 1*a*). To date, images derived from detectors located in the imaging plane have only been reported for the scanning confocal electron microscopy (SCEM) mode (Frigo *et al.*, 2002; Zaluzec, 2003; Zaluzec *et al.*, 2009; Nellist *et al.* 2006; Takeguchi *et al.*, 2008). SCEM uses a pinhole aperture to omit electrons that are not focused precisely on the imaging plane and thereby selects only those electrons that have undergone effectively zero net change in a transverse position. In this way, SCEM is able to obtain information about the specimen structure along the direction of the electron beam, and the technique has found powerful application in imaging structures embedded in thick specimens, albeit at relatively low resolution (Frigo *et al.*, 2002). In the R-STEM mode, on the other hand, no aperture is employed, so the full real-space distribution of electrons is accessible and is selected through the choice of detector geometry and the magnifying optics.

We used a Titan[3] 80–300 microscope fitted with pre- and post-specimen spherical-aberration correctors and operating at 300 kV. The microscope is equipped with a scan–descan system that keeps the beam steady on the detector and thus enables images to be obtained by rastering the beam (as opposed to translating the specimen). This can be important even for atomic resolution imaging, as the beam movement at the detector can be the order of a millimetre even when a sufficiently large magnification is used. The experiments were performed with a probe-forming aperture semi-angle of ∼17 mrad, to generate a probe size of ∼1 Å. Disc- and annular-shaped detectors were employed, with the diameter of the disc detector being about 1/5 of the inner diameter of the annular detector. The magnifying optics could be adjusted to effectively change the diameter of the detectors, and we observed atomic resolution contrast for the inner diameters of the annular detector at the specimen plane ranging from 30 to 4600 nm. Typical disc and annular R-STEM atomic resolution images are shown in Fig. 1(*b*,*c*), taken with an inner annular diameter of 30 nm. The images were obtained from a wedge-shaped gold specimen in the ⟨111⟩ orientation and show the atomic columns as bright dots in the annular R-STEM image and dark dots in the disc R-STEM image. There is no contrast reversal as the thickness changes along the wedge, a behavior observed across a range of specimens as well as the full range of detector sizes.

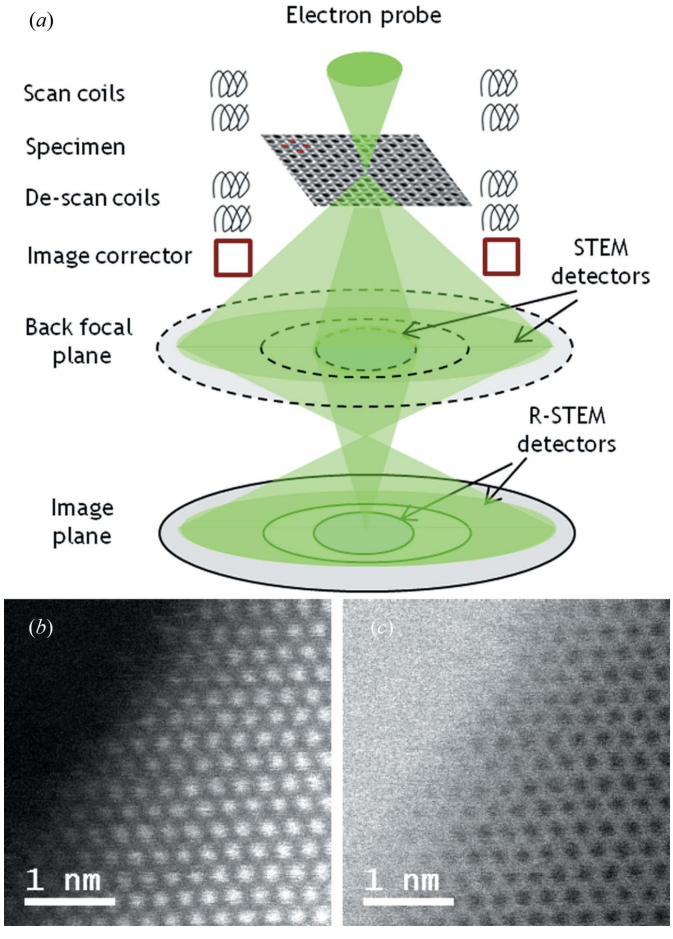

Figure 1
(*a*) Position of the detectors with respect to the image and diffraction plane in conventional bright-field/HAADF-STEM and disc and annular R-STEM. R-STEM images from the Au specimen in the ⟨111⟩ orientation. (*b*) Using an annular detector positioned in the image plane with an effective inner diameter of 30 nm. (*c*) Using a disc detector with an effective diameter of ∼6 nm.

Similar observations were made for a broad range of materials. For example, Fig. 2 shows R-STEM images of LaB_6 in the ⟨001⟩ orientation where, again, the heavy lanthanum atomic columns appear as white dots in the annular R-STEM image and as dark dots in the disc R-STEM image. However, in neither case can contrast from the boron octahedra be detected, even though the resolution is better than 1 Å and sufficient to resolve them. This behavior suggests that the disc R-STEM image contrast is complementary in nature to the annular R-STEM image (but cannot be exactly so, as there is a significant gap between the disc and annular detectors).

Further experiments involving focus changes (not shown) demonstrated a synchronized behavior of the contrast in the disc and annular R-STEM images without any evidence of contrast reversal. The detector sizes at the specimen plane were also varied, producing little change in the contrast but some change in the signal-to-noise ratio (SNR) of the images. Good contrast and SNR were observed in the annular R-STEM images across the large range of inner detector diameters stated above, which corresponds to an approximately 150-fold change in size. From this point of view, the R-STEM technique seems less sensitive than conventional HAADF-STEM, where a variation of only one order of magnitude in the camera length can strongly affect the image contrast and SNR.

In summary, our experimental observations indicate that both the disc and annular R-STEM images are 'incoherent', maintaining qualitatively complementary atomic resolution contrast across a range of specimen thicknesses, focus conditions and specimen types.

3. Discussions

To understand the contrast mechanism involved in R-STEM imaging, we first consider the case of the annular detector. In order for electrons to reach this detector they must undergo a minimum transverse displacement of at least 15–2300 nm, depending on the magnification used. Scattering by the specimen alone is insufficient to induce such a large displacement. For example, in the case of a specimen 10 nm thick, a relatively large scattering angle of 100 mrad will produce a transverse displacement at the specimen exit face of the order 1 nm. Hence there must be an additional mechanism involved. In a spherical-aberration-corrected imaging system, electrons that are scattered by the specimen to angles smaller than about 25 mrad will be accurately focused in the image plane. However, electrons scattered to higher angles will encounter significant higher-order aberrations, causing them to be displaced in the image plane, enabling them to reach the annular detector. This proposed mechanism was tested experimentally by introducing an aperture in the back focal plane of the objective lens to limit the angular range of the electrons going through the imaging system to 17 mrad. This action reduced the signal and contrast in the experimental annular R-STEM image effectively to zero, confirming the role of higher-order aberrations.

Based on this mechanism, a mathematical description of the R-STEM image intensity $I(\mathbf{x}_0)$ as a function of the probe position $\mathbf{x}_0$ is given by the expression (Dwyer *et al.*, 2011)

$$I(\mathbf{x}_0) = \int \mathrm{d}^2\mathbf{k}\, D(\mathbf{x}(\mathbf{k}))I(\mathbf{k}, \mathbf{x}_0). \qquad (1)$$

In this expression, bold symbols denote two-dimensional vectors perpendicular to the optic axis, $I(\mathbf{k}, \mathbf{x}_0)$ is the intensity of electrons at a point $\mathbf{k}$ in the diffraction plane, $\mathbf{x}(\mathbf{k})$ is the aberration-induced displacement experienced by such electrons at the image plane, and $D(\mathbf{x})$ is a function characterizing the R-STEM detector. Equation (1) is similar to an expression describing conventional STEM imaging except that the function $D(\mathbf{x}(\mathbf{k}))$ describes an 'effective' detector

operating in the diffraction plane. This effective detector describes the range of momenta of the electrons that are detected by the actual physical detector located in the image plane. The shape of the effective detector is determined by both the geometry of the physical detector and the aberrations of the post-specimen lens system. It should be noted that in deriving equation (1) the approximation is made that the effect of the post-specimen lens system is adequately described using geometric optics (the accuracy of this approximation is examined in Dwyer *et al.*, 2011).

In the case of annular R-STEM, the effective detector in equation (1) is an annulus in the diffraction plane (though its annular geometry will contain distortions associated with the aberrations). In this way, annular R-STEM shares many common features with conventional ADF-STEM: atomic contrast is generated in annular R-STEM images because when the electron probe is positioned on an atomic column, there is a greater probability of scattering to high angles *via* thermal diffuse and Rutherford scattering, and therefore a greater probability of electrons being displaced to the annular detector through higher-order aberrations. The images are incoherent both because of the largely incoherent nature of thermal diffuse scattering plus the additional phase-scrambling effect of the large effective detector.

In the case of disc R-STEM, the effective detector is a (distorted) disc in the diffraction plane (which, again, contains distortions associated with the lens aberrations). This effective disc detector is approximately complementary to the effective annular detector (in the sense that it collects electrons that pass through the hole in the effective annular detector). Hence, the incoherent nature of disc R-STEM images can be understood as a result of their approximate complementarity with annular R-STEM images, as observed.

Fig. 2(*c*) presents fully quantitative calculations of disc and annular R-STEM images based on equation (1). The calculations show images of LaB_6 in the [001] orientation for specimen thicknesses from 20 to 80 nm. The calculations incorporate dynamical electron scattering in the specimen using the multislice method (Dwyer *et al.*, 2011), including an accurate description of scattering to high angles caused by thermal diffuse scattering (Goodman & Moodie, 1974; Kirkland, 1998; Dwyer & Etheridge, 2003; Dwyer, 2010), performed using a modified version of the code described in Dwyer (2010). A disc detector diameter of 6 nm and annular detector inner and outer diameters of 30 and 185 nm were assumed. The aberration coefficients of the imaging system were set to $C_5 = 6.8$ mm, $|A5| = 3.1$ mm and $C_7 = 195$ mm, which are representative of residual high-order aberrations in a Cs-corrected imaging system (Haider, Rose *et al.*, 1998). It is seen that the qualitative agreement between the experimental and simulated images is excellent. Specifically, the experimentally observed incoherent nature of disc and annular R-STEM images, as described above, is well reproduced by the simulations. Moreover, this behavior is seen to apply to the entire range of specimen thicknesses considered. The consistency between the simulated and experimental images supports the interpretation of the R-STEM image contrast in terms of aberration-induced displacements.

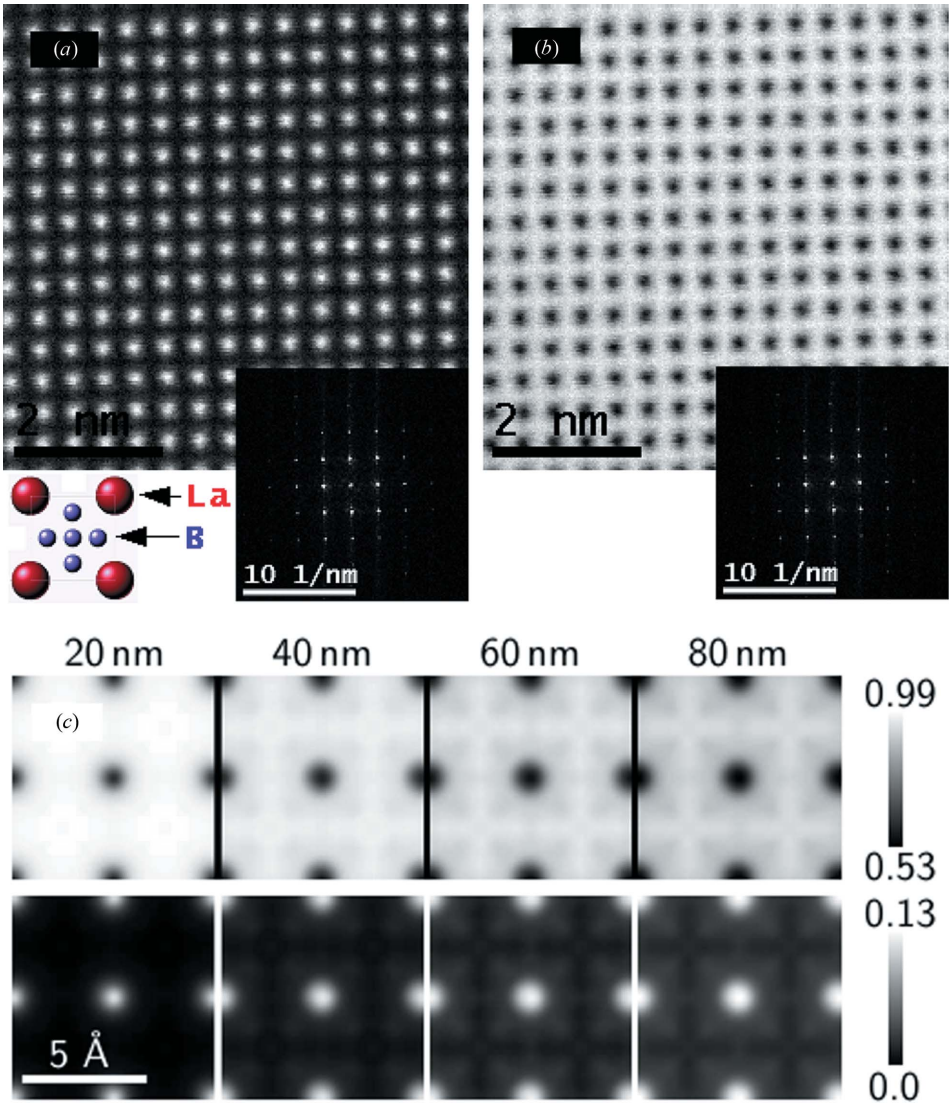

Figure 2
R-STEM images from an LaB_6 specimen in the ⟨100⟩ orientation. (*a*) Using an annular detector positioned in the image plane with an effective inner diameter of 30 nm. (*b*) Using a disc detector with an effective diameter of ∼6 nm. Fast Fourier transforms of the images are displayed in the insert as well as a projection of the unit cell. (*c*) Simulations of the disc (top row) and annular (bottom row) R-STEM images of ⟨001⟩-oriented LaB_6 for a range of specimen thicknesses (indicated at top). Each image shows 2 × 2 unit cells. The intensity scales (right) indicate the fraction of probe electrons detected.

4. Conclusions

In conclusion, we have demonstrated an atomic resolution incoherent imaging mode in scanning transmission electron microscopy using

detectors in real space, achieving a resolution comparable to conventional HAADF-STEM with good contrast. Both disc and annular R-STEM images are robust with respect to thickness, focus and detector diameters, and have been tested on a variety of materials. An imaging mechanism is proposed whereby the higher-order aberrations of the imaging system cause significant transverse displacements of the high-angle scattered electrons. A mathematical formulation of this mechanism involving the concept of an effective detector has been presented. Annular R-STEM images are understood to utilize the same electron–specimen interactions as conventional ADF-STEM, but the higher-order aberrations play an instrumental role in determining which electrons are detected. Disc R-STEM images offer a very high signal, incoherent imaging mode with good contrast and promising signal-to-noise characteristics, suggesting that this mode may be suitable as a low dose or very fast acquisition technique. A comprehensive quantitative analysis to assess the parameters that will optimize the signal-to-noise ratio of this mode is a subject for future work.

The authors would like to acknowledge useful discussions with Maximilian Haider and Peter Hartel from CEOS. SL and BF would like to thank Peter Tiemeijer (FEI) for helpful discussions on the contrast mechanism. JE and GAB are grateful to the Ontario MRI-ISOP funding. Experimental work presented here was performed at the Canadian Centre for Electron Microscopy – CCEM and at the Monash Centre for Electron Microscopy – MCEM. The CCEM is a national facility supported by the Natural Sciences and Engineering Research Council of Canada and McMaster University. Instrumentation used at MCEM was funded by the Australian Research Council infrastructure grant LE0454166 and supported by Monash University.

References

Crewe, A. V, Wall, J. & Welter, L. M. (1968). *J. Appl. Phys.* **39**, 5861–5868.
Dwyer, C. (2010). *Ultramicroscopy*, **110**, 195–198.
Dwyer, C. & Etheridge, J. (2003). *Ultramicroscopy*, **96**, 343–360.
Dwyer, C., Lazar, S., Chang, L. Y., Etheridge, J., Botton, G. A., Hartel, P. & Haider, M. (2011). In preparation.
Erni, R., Rossell, M. D., Kisielowski, C. & Dahmen, U. (2009). *Phys. Rev. Lett.* **102**, 096101.
Findlay, S. D., Saito, T., Shibata, N., Sato, Y., Matsuda, J., Asano, K., Akiba, E., Hirayama, T. & Ikuhara, Y. (2010). *Appl. Phys. Express*, **3**, 116603.
Findlay, S. D., Shibata, N., Sawada, H., Okunishi, E., Kondo, Y., Yamamoto, T. & Ikuhara, Y. (2009). *Appl. Phys. Lett.* **95**, 191913.
Frigo, S. P., Levine, Z. H. & Zaluzec, N. J. (2002). *Appl. Phys. Lett.* **81**, 2112.
Goodman, P. & Moodie, A. F. (1974). *Acta Cryst.* A**30**, 280–290.
Haider, M., Rose, H., Uhlemann, S., Schwan, E., Kabius, B. & Urban, K. (1998). *Ultramicroscopy*, **75**, 53–60.
Haider, M., Uhlemann, S., Schwan, E., Rose, H., Kabius, B. & Urban, K. (1998). *Nature (London)*, **392**, 768–769.
Jia, C. L., Thust, A. & Urban, K. (2005). *Phys. Rev. Lett.* **95**, 225506.
Jia, C. L. & Urban, K. (2004). *Science*, **303**, 2001–2004.
Kirkland, E. J. (1998). *Advanced Computing in Electron Microscopy*. New York: Plenum Press.
Kisielowski, C. *et al.* (2008). *Microsc. Microanal.* **14**, 469–477.
Krivanek, O. L., Chisholm, M. F., Nicolosi, V., Pennycook, T. J., Corbin, G. J., Dellby, N., Murfitt, M. F., Own, C. S., Szilagyi, Z. S., Oxley, M. P., Pantelides, S. T. & Pennycook, S. J. (2010). *Nature (London)*, **464**, 571–574.
Krivanek, O. L., Dellby, N. & Lupini, A. R. (1999). *Ultramicroscopy*, **78**, 1–11.
Nellist, P. D., Behan, G., Kirkland, A. I., Hetherington, C. J. D. (2006). *Appl. Phys. Lett.* **89**, 124105.
Nellist, P. D., Chisholm, M. F., Dellby, N., Krivanek, O. L., Murfitt, M. F., Szilagyi, Z. S., Lupini, A. R., Borisevich, A., Sides, W. H. & Pennycook, S. J. (2004). *Science*, **305**, 1741.
Sawada, H., Hosokawa, F., Kaneyama, T., Ishizawa, T., Terao, M., Kawazoe, M., Sannomiya, T., Tomita, T., Kondo, Y., Tanaka, T., Oshima, Y., Tanishiro, Y., Yamamoto, N. & Takayanagi, K. (2007). *Jpn. J. Appl. Phys.* **46**, L568–L570.
Takeguchi, M., Hashimoto, A., Shimojo, M., Mitsuishi, K. & Furuya, K. (2008). *J. Electron Microsc.* **57**, 123–127.
Zaluzec, N. J. (2003). US Patent 6 548 810.
Zaluzec, N. J., Weyland, M. & Etheridge, J. (2009). *Microsc. Microanal.* **15**, 614–615.